POLITECNICO DI TORINO
Repository ISTITUZIONALE

VHCF strength decrement in large H13 steel specimens subjected to ESR process

Original
VHCF strength decrement in large H13 steel specimens subjected to ESR process / Tridello, Andrea; Paolino, Davide Salvatore; Chiandussi, Giorgio; Rossetto, Massimo. - In: PROCEDIA STRUCTURAL INTEGRITY. - ISSN 2452-3216. - ELETTRONICO. - 2:(2016), pp. 1117-1124. [10.1016/j.prostr.2016.06.143]

Availability:
This version is available at: 11583/2656686 since: 2016-11-21T10:54:27Z

Publisher:
ELSEVIER

Published
DOI:10.1016/j.prostr.2016.06.143

Terms of use:

This article is made available under terms and conditions as specified in the corresponding bibliographic description in the repository

Publisher copyright

(Article begins on next page)

12 October 2024

Available online at www.sciencedirect.com

ScienceDirect

Procedia Structural Integrity 2 (2016) 1117–1124

Structural Integrity Procedia

www.elsevier.com/locate/procedia

21st European Conference on Fracture, ECF21, 20-24 June 2016, Catania, Italy

VHCF strength decrement in large H13 steel specimens subjected to ESR process

A. Tridello[a]*, D.S. Paolino[a], G. Chiandussi[a], M. Rossetto[a]

[a]*Department of Mechanical and Aerospace Engineering, Politecnico di Torino, Turin, Italy*

Abstract

Failures at very high number of cycles (Very-High-Cycle Fatigue, VHCF) generally originate from inclusions or defects present within the material. VHCF response of materials is therefore strongly affected by the defect population and, in particular, by the characteristic defect size, which statistically increases with the material volume. According to this well-known dependency, Size Effects were found to significantly affect the VHCF strength of high-strength steels.
The paper aims at assessing the influence of Size Effects on the VHCF response of a high performance AISI H13 steel subjected to Electro Slag Remelting (ESR) refinement process. Ultrasonic VHCF tests were carried on specimens characterized by different loaded volumes (hourglass and Gaussian specimens). Experimental results showed that Size Effects strongly influences the VHCF response of the investigated high performance steel, even if it is characterized by a high degree of purity and by a population of inclusions with limited size.

Copyright © 2016 The Authors. Published by Elsevier B.V. This is an open access article under the CC BY-NC-ND license (http://creativecommons.org/licenses/by-nc-nd/4.0/).
Peer-review under responsibility of the Scientific Committee of ECF21.

Keywords: Veri High Cycle Fatigue (VHCF); ultrasonic tests; Electro Slag Remelting (ESR); Size Effects.

1. Introduction

The continuous increment of the required design lifetime of many machinery components and the experimental evidence that materials could fail at stress amplitudes below the conventional fatigue limit led to a growing interest in the study of the Very-High-Cycle Fatigue (VHCF) behavior of materials. Experimental results showed that in the VHCF regime cracks generally nucleate around defects or inclusions present within the material (internal

* Corresponding author. Tel.: +39 011 090 6913.
E-mail address: andrea.tridello@polito.it

Copyright © 2016 The Authors. Published by Elsevier B.V. This is an open access article under the CC BY-NC-ND license (http://creativecommons.org/licenses/by-nc-nd/4.0/).
Peer review under responsibility of the Scientific Committee of ECF21.
10.1016/j.prostr.2016.06.143

nucleation). Therefore, VHCF response of materials is strongly affected by the defect population and, in particular, by the characteristic defect size, which statistically increases with the material volume. According to this well-known dependency, Size Effects (SE) were found to significantly affect the VHCF strength of materials, and, in particular, of high-strength steels (Murakami, 2002; Furuya, 2008; Furuya, 2010, Furuya, 2011; Sun et al., In press). Experimental tests showed that the larger the tested risk-volume V_{90} (volume of material subjected to a stress amplitude larger than the 90% of the maximum stress according to [Furuya, 2011]) the smaller is the VHCF strength. In (Furuya, 2011), a 20% strength decrement was found by increasing the specimen risk-volume from 33 mm^3 to 900 mm^3.

SE on the VHCF response of a pure AISI H13 steel subjected to Electro Slag Remelting (ESR) process are investigated and discussed in the present paper. Fully reversed tension-compression tests are carried out on hourglass specimens (risk-volume smaller than 200 mm^3) and on Gaussian specimens (risk-volume larger than 2300 mm^3) by using the ultrasonic testing machines developed at Politecnico di Torino. Fracture surfaces are observed with a Scanning Electron Microscope (SEM) in order to determine crack origin. All the internal failures originated from small inclusions present within the material: the chemical composition and the shape of the inclusions in hourglass and in Gaussian specimens are analyzed and compared in the paper. In order to estimate the P-S-N curves and the fatigue limit variation as a function of the tested volume, experimental results are finally analyzed according to a statistical model recently developed by the authors (Paolino et al., In press) and based on the hydrogen embrittlement theory (Murakami, 2002). SE were found to significantly influence the VHCF response of the tested high performance steel, even if the ESR process allows for removing large inclusions and impurities and to significantly enhance the steel cleanliness.

Nomenclature

V_{90}	Volume of material subjected to a stress amplitude larger than the 90% of the maximum stress
σ_{real}	Local stress amplitude in the vicinity of the initial inclusion
$\sqrt{a_{d,0}}$	Square root of the projected area of the inclusion originating the failure
V_{real}	Real-volume associated to each specimen
$F_n\left(\sqrt{a_{d,0}}\right)$	Type 1 LEV cumulative distribution function
$f_n\left(\sqrt{a_{d,0}}\right)$	Type 1 LEV probability density function
$f_n\left(\sqrt{a_{d,0}}\middle\vert\sqrt{a_{d,0}} > 0\right)$	truncated Type 1 LEV probability density function
$L(\cdot)$	Maximum likelihood function

2. Materials

Experimental tests are carried out on AISI H13 steel (EN 40CrMOV5-1 steel according to the UNI EN ISO 4957) obtained by conventional casting and thereafter subjected to Electro Slag Remelting (ESR) process. The controlled solidification obtained through the ESR process allows for removing the largest inclusions and impurities from the remelted material, thus significantly enhancing the steel cleanliness. The entire ESR process is performed in a protective atmosphere, in order to limit the hydrogen absorption during the second remelting and to increase furthermore the steel cleanliness.

AISI H13 is classified as a hot work tool steel, but it is also used for components subjected to very high number of cycles and therefore prone to VHCF failures, e.g. for the production of components of fuel injection systems for naval engines or for aerospace components (landing gears). The chemical composition of the investigated steel is reported in Table 1.

Table 1. Chemical composition of the investigated H13 ESR

Element	C	Si	Mn	Cr	Mo	V
Mass (%)	0.39	1.0	0.4	5.2	1.4	0.9

Experimental tests are carried out on hourglass specimens ($V_{90} = 194\ \mathrm{mm}^3$) and Gaussian specimens ($V_{90} = 2300\ \mathrm{mm}^3$) characterized by significantly different V_{90} in order to highlight the SE for the investigated material. Hourglass and Gaussian specimens are designed according to (Tridello et al., 2013; Paolino et al, 2014). The stress concentration factor is verified to be smaller than 1.08 through Finite Element Analysis. Fig. 1 shows the geometry of hourglass and Gaussian specimens used for the experimental tests.

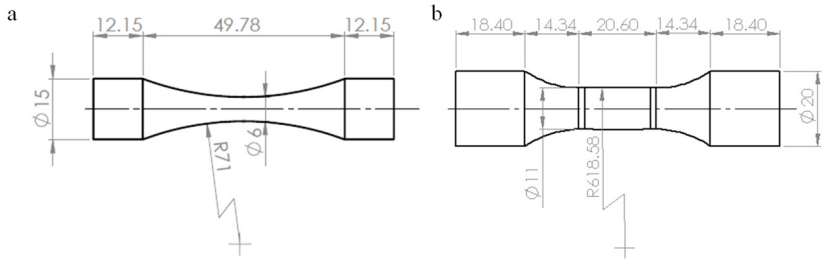

Fig. 1. Geometry of specimens used for experimental tests: (a) hourglass specimen; (b) Gaussian specimen.

Specimens are manufactured through a CNC machining process starting from rectangular bars with dimensions 32x32x115 mm. After the machining process, specimens are quenched and tempered with the ordinary industrial cycle in a vacuum furnace in order to obtain a homogeneous tempered martensite microstructure. The heat treatment involved preheating at 1023 K, austenitizing at 1030 K, gas quenching and three tempering cycles: first tempering at 793 K, second and third tempering at 813 K. The tensile strength and the Vickers hardness of the investigated material after the heat treatment are 2100 MPa and 560 HV, respectively.

Specimens are finally fine polished in order to avoid surface nucleation of cracks around defects which could form during the machining process.

3. Experimental tests

Experimental tests are carried out by using the ultrasonic testing machines for fully reversed tension-compression tests developed at the Politecnico di Torino (Paolino et al., 2012; Tridello et al., 2015). Tests are carried out at constant stress amplitude: a closed loop control based on the displacement measured with a laser displacement sensor at the specimen free end is implemented in order to control the stress amplitude. An accurate strain gage calibration is performed to correlated the measured displacement amplitude and the stress amplitude in the specimen center.

Intermittent tests (Stanzl-Tschegg, 2014) are carried out in order to limit the temperature increment due to internal heat generation (Tridello et al., 2015)] Specimen temperature is monitored in real-time during the experimental tests with an infrared sensor and is maintained in the range 303 K – 323 K. Three vortex tubes are employed to slow down the temperature increment and to speed up the specimen cooling phase.

Temperature distribution in the Gaussian specimen part is also evaluated with a thermocamera. Temperature variation in the Gaussian specimen part is verified to be smaller than 1%. Temperature variation within the specimen cross-section, verified through Finite Element Analysis, is found to be smaller than 2%. In this respect, temperature in the Gaussian specimen part is considered uniform during the experimental tests.

4. Experimental results

VHCF tests are carried out up to failure or up to 10^{10} cycles (runout specimen). Hourglass specimens are subjected to a stress amplitude ranging from 630 MPa to 820 MPa; Gaussian specimens are subjected to a stress amplitude ranging from 570 MPa to 800 MPa. Fracture surfaces are observed with a Scanning Electron Microscope (SEM) in order to determine crack origin. 13 out of 17 hourglass specimens failed due to internal nucleation of cracks around non-metallic inclusions; one hourglass specimen failed due to a surface crack. 16 out of 19 Gaussian specimens failed due to internal cracks originating from non-metallic inclusions; one Gaussian specimen failed due to a surface crack. In the following analysis, only internal failures are considered.

In Section 4.1, the distribution of inclusions originating failures is analyzed in order to assess the stress amplitude in the vicinity of the initial defect. In Section 4.2, the chemical composition and the shape of inclusions originating failures in hourglass and in Gaussian specimens are compared and the statistical distribution of inclusion size is estimated. Finally, the experimental data are analyzed according to the model proposed in (Paolino et al., In press) and based on the hydrogen embrittlement theory (Murakami, 2002). In (Paolino et al., In press), an additional stress intensity factor proportional to the hydrogen concentration in the vicinity of the ODA is added to the stress intensity factor associated to the inclusion in order to model the hydrogen assistant crack growth. Following the procedure proposed in (Paolino et al., In press), the P-S-N curves and the fatigue limit variation as a function of the material volume are finally estimated in Section 4.3.

4.1. Real stress

The local stress amplitude in the vicinity of the initial inclusion is assessed by considering its exact location in the specimen. Fig. 2 shows the distribution of inclusions originating failures within the specimen volume. The distribution of inclusions along the longitudinal direction (abscissa axis) is plotted with respect to their location in the radial direction.

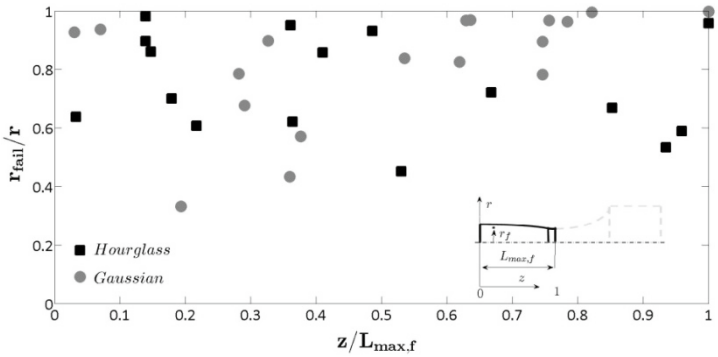

Fig. 2. Location of the initial inclusion in longitudinal and radial directions.

Failures are uniformly distributed in hourglass and in Gaussian specimens, thus confirming the validity of the experimental results. Therefore, in particular for Gaussian specimens, the limited temperature variation within the Gaussian specimen part did not affect the experimental results.

The local stress in the vicinity of the initial inclusion (σ_{real}) is determined through Finite Element Analysis (FEA). Differently from the literature (Furuya, 2011), σ_{real} is considered as the applied stress in the following analysis, in order to take into account the stress variation within the specimen volume. Fig. 3 shows the S-N plot of the experimental dataset, obtained by considering σ_{real}.

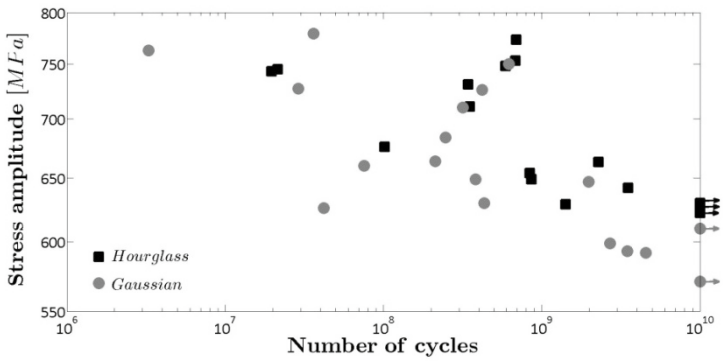

Fig. 3. S-N plot of the experimental dataset.

4.2. Inclusion analysis

All fracture surfaces exhibit a fish-eye morphology, with the Optical Dark Area (ODA) in the vicinity of the inclusion originating failure (Murakami, 2002). According to the hydrogen embrittlement theory, crack grows within the ODA with the assistance of hydrogen and then it propagates starting from the border of the ODA without the hydrogen assistance. Therefore, the ODA differentiates between the crack growth with the assistance of hydrogen and the crack propagation without the hydrogen assistance (Murakami, 2002). Fig. 4 shows a typical fish-eye morphology in a failed Gaussian specimen.

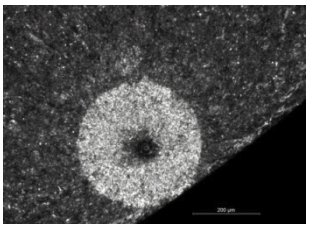

Fig. 4. Fish-eye fracture (Gaussian H13 ESR steel, $\sigma = 647$ MPa at $1.98 \cdot 10^9$ cycles).

The chemical composition of inclusions originating failures is determined through Energy-dispersive X-ray spectroscopy. Inclusions in hourglass and in Gaussian specimens are characterized by the same chemical composition. All fatigue failures originated from non-metallic oxide type inclusions containing high percentage of Aluminium, Calcium and Manganese.

Inclusions originating failures are generally spherical both in hourglass and Gaussian specimens. A cluster of inclusions is at the origin of the fatigue crack in one hourglass specimen and in two Gaussian specimens. Since no relevant difference is found in the chemical composition and in the shape of initial inclusions, the population of inclusions in hourglass and in Gaussian specimens is considered the same.

Inclusion size in hourglass and in Gaussian specimen is finally compared: according to (Murakami, 2002), the square root of the projected area of the inclusion, $\sqrt{a_{d,0}}$, is considered as the characteristic defect size. Table 2 compares the smallest ($\sqrt{a_{d,0}}_{min}$) and the largest inclusion ($\sqrt{a_{d,0}}_{max}$) in hourglass and Gaussian specimens.

Table 2. Inclusion size in hourglass and in Gaussian specimens.

Specimen type	$\sqrt{a_{d,0}}_{min}$ [μm]	$\sqrt{a_{d,0}}_{max}$ [μm]
Hourglass	10	23
Gaussian	15	31

As expected and according to (Murakami, 2002; Furuya, 2011), inclusions in hourglass specimens are generally smaller than inclusions in Gaussian specimens. The largest inclusion in Gaussian specimens is about two times larger than the largest inclusion in hourglass specimens.

According to (Paolino et al., In press), in order to estimate the fatigue limit and the P-S-N curves (Section 4.3), the statistical distribution of inclusion size must be determined. According to (Murakami, 2002), inclusion size is assumed to follow a Type 1 Largest Extreme Value Distribution (LEVD). Runout specimens are tested at higher stress amplitude in order to determine the largest inclusion size within the loaded volume.

In the literature, V_{90} is arbitrary assumed as the volume associated to the tested specimens for the estimation of the LEVD parameters (Murakami, 2002; Furuya, 2011). However, if V_{90} is taken into account, it is possible that the inclusion originating failure is not the largest inclusion within V_{90} (i.e., inclusions with different sizes are subjected to different stress amplitude). The arbitrary choice of V_{90} can therefore lead to an incorrect evaluation of the volume at risk and, consequently, to inaccuracy in the estimated inclusion size distribution.

In the paper, the *real-volume* (V_{real}) is considered as the volume associated to each tested specimen. The *real-volume* is defined as the volume of material subjected to a stress amplitude larger than the stress amplitude evaluated

at the inclusion location. For each inclusion originating failure, the corresponding V_{real} can be defined. Therefore, there is no need to arbitrarily assume the V_{90} as the volume at risk: the *real-volume* allows for taking into account the actual volume associated to each inclusion and therefore permits a more proper estimation of the inclusion size distribution.

V_{real} for each failed specimen is computed through FEA. The minimum V_{real} found experimentally is equal to 3 mm^3 (hourglass specimens) and the maximum *real-volume* is equal to 1914 mm^3 (Gaussian specimens). The LEVD parameters are estimated by considering V_{real} and by applying the Maximum Likelihood Principle.

In particular, if $V_{real,0}$ is the reference volume (i.e., the smallest V_{real} tested), the probability of having an inclusion with size smaller than $\sqrt{a_{d,0}}$ in a *real-volume* n times larger than $V_{real,0}$ (i.e, $n = \frac{V_{real}}{V_{real,0}}$) is expressed by:

$$F_n\left(\sqrt{a_{d,0}}\right) = \left\{\exp\left[-\exp\left(-\frac{\sqrt{a_{d,0}}-\mu_{\sqrt{A}}}{\sigma_{\sqrt{A}}}\right)\right]\right\}^n, \tag{1}$$

where $\mu_{\sqrt{A}}$ and $\sigma_{\sqrt{A}}$ are the location and the scale parameter of the LEVD.
The probability density function of the LEVD can be obtained by differentiating $F_n\left(\sqrt{a_{d,0}}\right)$ with respect to $\sqrt{a_{d,0}}$:

$$f_n\left(\sqrt{a_{d,0}}\right) = n \cdot \left[F\left(\sqrt{a_{d,0}}\right)\right]^{n-1} f_1\left(\sqrt{a_{d,0}}\right). \tag{2}$$

Since $\sqrt{a_{d,0}}$ must be larger than 0, the truncated probability density function ($f_n\left(\sqrt{a_{d,0}}\middle|\sqrt{a_{d,0}} > 0\right) = \frac{f_n\left(\sqrt{a_{d,0}}\right)}{1-F_n\left(\sqrt{a_{d,0}}\right)}$) is considered for the parameter estimation. The Likelihood function $L(\lambda, \delta\ )$ is expressed by:

$$L(\lambda, \delta\ ) = \prod_{i=1}^{n_s} f_{n_i}\left(\sqrt{a_{d,0}}_i\middle|\sqrt{a_{d,0}} > 0\right), \tag{3}$$

where $f_{n_i}\left(\sqrt{a_{d,0}}_i\middle|\sqrt{a_{d,0}} > 0\right)$ is the truncated probability density function evaluated at the i-th inclusion size $\sqrt{a_{d,0}}_i$ and at the i-th ratio n_i (i.e., $n = \frac{V_{real,i}}{V_{real,0}}$), with $i = 1 \ldots n_s$, being n_s the number of tested specimens.

The numerical maximization is carried out in Matlab® through an internal algorithm based on the *simplex search* method. The estimates of the parameters $\mu_{\sqrt{A}}$ and $\sigma_{\sqrt{A}}$ are equal to 2.18 µm and 3.2 µm, respectively.

4.3. P-S-N curves and fatigue limit

P-S-N curves are estimated according to the procedure described in (Paolino et al., In press) and by taking into account the statistical distribution of $\sqrt{a_{d,0}}$ estimated in Section 4.2.

Fig. 5 shows the P-S-N curves evaluated at the smallest *real-volume* ($V_{real,min}$). The estimated 0.5-th and 0.025-th P-S-N curves are shown in the graph.

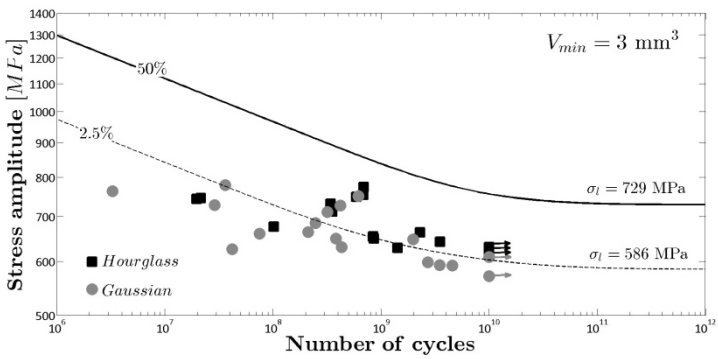

Fig. 5. P-S-N curves estimated at the smallest V_{real}.

Fig. 6 shows the P-S-N curves evaluated at the largest *real-volume* ($V_{real,max}$). The estimated 0.5-th and 0.025-th P-S-N curves are shown in the graph.

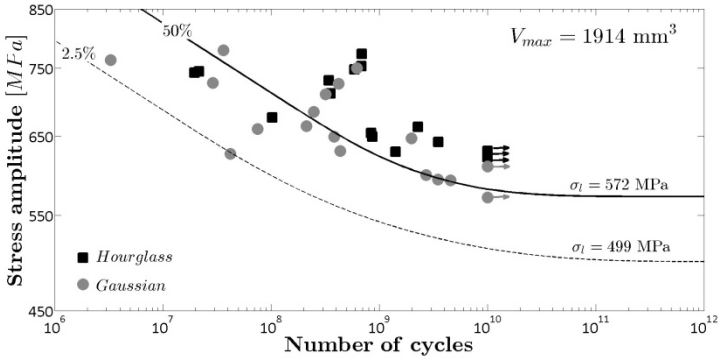

Fig. 6. P.S-N curves evaluated at the largest V_{real}.

A significant difference exists between the P-S-N curve evaluated at the smallest and at the largest tested *real-volume*. In Fig. 5, all failures are below the 50% P-S-N curve. In particular, if the Gaussian specimens are considered, 11 out of 16 failures are below the 2.5% P-S-N curve. On the contrary, in Fig. 6, all failures are above the 2.5% P-S-N curve and about the 50% of failures are above the 50% P-S-N curve.

The fatigue limit variation with respect to the tested *real-volume* is shown in Fig. 7.

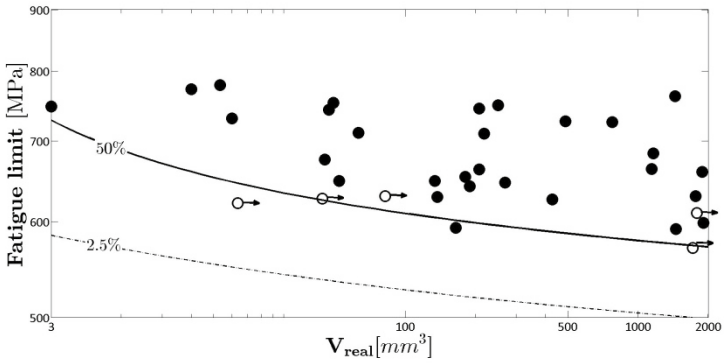

Fig. 7. Fatigue limit variation as a function of the tested V_{real}.

According to Fig. 7, the model proposed in (Paolino et al., In press) is in agreement with the experimental data. Only 1 failure out of 29 is below the 0.5-th quantile. No failure occurs below the 2.5% fatigue limit curve. The fatigue limit decreases significantly as the *real-volume* increases. In particular, for the smallest *real-volume* (3 mm^3), the 0.5-th quantile of the fatigue limit is equal to 729 MPa, while for the largest *real-volume* (1914 mm^3) the 0.5-th quantile of the fatigue limit is equal to 572 MPa, with a 21% reduction. Therefore, even if the H13 ESR steel is characterized by a high degree of purity and by a population of defects with limited size (i.e., inclusions in H13 steel not subjected to ESR process are larger than 50 μm [Tridello et al., 2015]), SE are relevant and lead to a significant decrement of the VHCF strength.

In (Furuya, 2011), two V_{90} (33 mm^3 and 900 mm^3) were considered for investigating SE. The fatigue limit variation was obtained by imposing the passage of an arbitrary exponential function between two experimental points. The trend obtained in (Furuya, 2011) is confirmed by the experimental results for the H13 ESR steel. However, in this paper the fatigue limit variation curve is estimated by considering a large number of experimental points (34) and by testing specimens characterized by larger risk-volumes. Moreover, according to the model proposed in (Paolino et al., In press), the scatter of the fatigue limit curve is also estimated. P-S-N curves and fatigue

limit curves at different failure probabilities can therefore be considered as the design curves when components with large volumes are designed.

5. Conclusions

Ultrasonic tests were carried out in order to evaluate SE on the VHCF response of an AISI H13 steel subjected to the ESR refinement process and characterized by a high degree of cleanliness. Fully reversed tension compression tests were carried out on hourglass and Gaussian specimens characterized by different risk-volumes. The experimental data were analyzed according to the model recently proposed in (Paolino et al., In press) and based on the hydrogen embrittlement theory proposed by Murakami (Murakami, 2002).

Inclusions originating failure in hourglass and Gaussian specimens were compared. SEM analysis revealed that the inclusion population was the same in hourglass and in Gaussian specimens (i.e., they were characterized by the same chemical composition and the same shape). However, as expected and according to (Murakami, 2002; Furuya, 2011), inclusions in hourglass specimens were generally smaller than inclusions in Gaussian specimens, due to the different risk-volume of the tested specimens.

The distribution of defect size was also estimated. Differently from the literature, the actual volume associated to each inclusion, V_{real}, was considered for the estimation of the parameters of the defect size distribution.

P-S-N curves at different V_{real} and fatigue limit variation as a function of V_{real} were finally estimated in the paper. A 21% reduction of the fatigue limit was found by considering the smallest and the largest tested V_{real}. Therefore, SE were found to significantly affect the VHCF response of the tested high performance H13 ESR steel, even if it is characterized by a high degree of cleanliness and by a population of inclusions with limited size (i.e., the largest inclusion experimentally found was equal to 31 μm).

The fatigue limit variation as a function of the material volume obtained in the literature (Furuya, 2011) is confirmed by the experimental results obtained by testing the H13 ESR steel. However, differently from the literature (Furuya, 2011), where only two experimental data were considered, in this paper the fatigue limit variation as a function of the material volume was obtained by considering a large number of experimental data and by testing specimens with larger risk-volumes, allowing for a more reliable estimation of SE in VHCF.

Acknowledgements

The authors would like to thank the research group of Prof. D. Firrao for the valuable suggestions concerning the material choice and the applied heat treatment.

References

Murakami, Y., 2002. Metal Fatigue: Effects Of Small Defects And Nonmetallic Inclusions. Elsevier, Oxford.

Furuya, Y., 2008. Specimen size effects on gigacycle fatigue properties of high-strength steel under ultrasonic fatigue testing. Scripta Mater. 58, 1014–1017.

Furuya, Y., 2010. Size effects in gigacycle fatigue of high-strength steel under ultrasonic fatigue testing. Procedia Eng. 2, 485–490.

Furuya, Y., 2011. Notable size effects on very high cycle fatigue properties of high strength steel. Mater. Sci. Eng. A 528, 5234–5240.

Sun, C., Zhang, X., Liu, X., Hong, Y., In press. Effects of specimen size on fatigue life of metallic materials in high-cycle and very-high-cycle fatigue regimes Fatigue Fract. Eng. Mater. Struct. DOI: 10.1111/ffe.12415.

Paolino, D.S., Tridello, A., Chiandussi, G., Rossetto, M., In press. S-N curves in the very-high-cycle fatigue regime: statistical modeling based on the hydrogen embrittlement consideration. Fatigue Fract. Eng. Mater. Struct., DOI: 10.1111/ffe.12431.

Tridello, A., Paolino, D.S., Chiandussi, G., Rossetto, M., 2013. Comparison between dog-bone and Gaussian specimens for size effect evaluation in gigacycle fatigue, Frattura e Integrità Strutturale 26, 49-56.

Paolino, D.S., Tridello, A., Chiandussi, G., Rossetto, M., 2014. On specimen design for size effect evaluation in ultrasonic gigacycle fatigue testing. Fatigue Fract. Eng. Mater. Struct. 5, 570-579.

Paolino, D.S., Rossetto, M., Chiandussi, G., Tridello, A., 2012. Sviluppo di una macchina a ultrasuoni per prove di fatica gigaciclica. 41th AIAS Conference, Vicenza (In Italian).

Tridello, A., Paolino, D.S., Chiandussi, G., Rossetto, M., 2015. VHCF response of AISI H13 steel: Assessment of size effects through Gaussian specimens, Procedia. Eng 109, 121-127.

Stanzl-Tschegg, S., 2014. Very high cycle fatigue measuring techniques. Int. J. Fatigue 60, 2-17.

Tridello, A., Paolino, D.S., Chiandussi, G., Rossetto, M., 2016. Gaussian specimens for VHCF tests: Analytical prediction of damping effects, Int. J. Fatigue 83, 36-41.